Investigation about iron(III) incorporation into layered double hydroxides: Compositional and structural properties of Mg2FeyAl(1–y)(OH)6-Cl and Zn2FeyAl(1–y)(OH)6-Cl

Mariana Pires Figueiredo, Alfredo Duarte, Victor Vendruscolo, Rodolphe Thirouard, Vera R.L. Constantino, Christine Taviot-Guého

Investigation about iron(III) incorporation into layered double hydroxides: compositional and structural properties of $Mg_2Fe_yAl_{(1-y)}(OH)_6$-Cl and $Zn_2Fe_yAl_{(1-y)}(OH)_6$-Cl

Mariana Pires Figueiredo[a], Alfredo Duarte[a], Victor Vendruscolo[a], Rodolphe Thirouard[b], Vera R. L. Constantino[a], Christine Taviot-Guého[b,].*

[a]Departamento de Química Fundamental, Instituto de Química, Universidade de São Paulo - USP, Av. Prof. Lineu Prestes 748, 05508-000, São Paulo, São Paulo, Brazil.

[b]Institut de Chimie de Clermont-Ferrand, UMR-CNRS 6296. Université Clermont Auvergne. Campus des Cézeaux, 24 avenue des Landais. B.P. 800 26. 63171 Aubière, France.

*corresponding author: Christine Taviot-Guého, christine.taviot-gueho@uca.fr

ABSTRACT

Layered Double Hydroxides (LDH) and related nanocomposites have attracted much attention for biomedical applications and the development of LDH drug carriers composed by endogenous metals, such as iron, is of obvious interest. However, most of the studies reported so far on iron-containing LDH, mainly focusing on the applications, suffer from insufficient data about the synthesis and the characterization of these materials. In this study, it is addressed compositional and structural properties of two series of LDH materials, $Mg_2Fe_yAl_{(1-y)}$-Cl and $Zn_2Fe_yAl_{(1-y)}$-Cl with a M^{2+}/M^{3+} molar ratio equal to 2 and $0 \leq y \leq 1$. By combining crystal-chemical reasoning, Rietveld refinements and pair distribution function analysis (PDF), it was possible to differentiate between contributions from crystalline and amorphous components. Concerning Mg-series, for $y > 0.5$, the compositions were found to slightly deviate from those expected with an increase in the value of R tending to 3. For Zn-series, more heterogeneous samples were obtained with the presence of amorphous 2-line ferrihydrite clearly demonstrated by PDF analysis. As well as providing a reliable approach to the characterization of Fe-LDH, this study gives useful elements for better understanding and interpreting the results reported in the literature regarding these phases.

KEYWORDS: Layered Double Hydroxides, iron incorporation, proper composition determination, biomaterials, solid-solution, Rietveld refinements, hydrotalcite supergroup

1. INTRODUCTION

Layered Double Hydroxides (LDH) represented by the general formula $[M^{3+}_{(1-x)}M^{2+}_{x}(OH)_2](A^{n-})_{x/n}.zH_2O$ and often abbreviated as $M^{2+}_{R}M^{3+}$-A^{n-} (where R is the molar ratio between the di and trivalent cations) have been considered as technologically promising materials for diverse and essential applications, particularly in health [1], catalysis [2], energy generation and storage [3], photodetection [4], and environment related fields [5]. The constantly increasing interest in these materials first stems from their low cost and easy preparation, and the considerable number of distinct chemical compositions that can be achieved. LDH applicability in biological, medicinal, and pharmaceutical topics is based on their flexible two-dimensional (2D) structure and their tunable exchange properties allowing storage and delivery of different types of A^{n-} bioactive anionic species. Thereby, drugs such as non-steroidal anti-inflammatories [6] or anticarcinogenics [7], and biomolecules like aminoacids [8] and even deoxyribonucleic acid segments [9] have been intercalated into LDH. Moreover, LDH hydroxide layers can be composed or doped with different M^{2+} and M^{3+} cations giving rise the possibility of choosing the most suitable chemical composition for the desired purpose [10].

For biological applications, LDH composed of Mg^{2+} or Zn^{2+} and Al^{3+} cations are frequently employed. Aluminum ion contact with human body widely occurs orally, such as with the consume of antiacids, which exposure to the gastrointestinal is mild [11]. In fact, the antiacid Talcid® [12] patented by Bayer AG, composed of LDH containing Mg^{2+} and Al^{3+} cations and intercalated with CO_3^{2-} anions, not only chemically neutralizes gastric acids but also has shown to induce the expression of epithelial growth factor and its receptor in normal gastric mucosa and also in ulcer scar

promoting mucosa restauration [13,14]. Besides, it has been shown that cations from Talcid® are not absorbed by the intestine [15]. However, the contact with the systemic route when used in the form of aluminum oxyhydroxide, for example as adjuvant of vaccines intravenously administered to promote the immune response, clearly shows toxicity [16]. Although *in vitro* and *in vivo* studies have not indicated possible toxicity of Al-LDH, there is a lack of studies about aluminum effect considering long-term treatments and dose-dependency [17,18]. Moreover, Al^{3+} absorption has been associated to neurotoxicity and general tissues accumulation [16,19].

For all these reasons, the partial or complete substitution of aluminum by endogenous metals, such as iron, is desirable to improve the biocompatibility of LDH materials. Recently, some of us have reported biocompatibility studies conducted on iron containing LDH [24,25]. Two LDH materials composed of magnesium or zinc as divalent cations and a mixture of Fe^{3+} and Al^{3+} in the same proportion as trivalent cations, *i.e.* $Mg_2Fe_{0.5}Al_{0.5}$ and $Zn_2Fe_{0.5}Al_{0.5}$, and intercalated with chloride anions were examined through intramuscular implants in rats. The modulation of collagen production was observed during tissue regeneration process depending on the nature of the cations combined in LDH layers. Type-I collagen was predominant in the presence of iron for both $Mg_2Fe_{0.5}Al_{0.5}$-Cl and $Zn_2Fe_{0.5}Al_{0.5}$-Cl compositions. Comparatively, for Mg_2Al-Cl and Zn_2Al-Cl compositions, collagen formation was guided by the divalent cation nature and a predominance of type-III collagen was observed for the Zn_2Al matrix [20]. Other studies have also evaluated the performance of Mg_RFe-LDH as phosphate binding agent for oral administration [22], for enzyme adsorption [23], and also as osteogenesis enhancers by covering Ti plates [24], bone [25], and orthopaedic implants [26] with LDH. Balcomb et al. [27] reported the use of Mg_RAl, Mg_RFe and Zn_RFe LDH as nonviral gene delivery vehicles; all samples showed low cytotoxicity

against HEK293 cells with viability over 100 % and the highest values were observed for Fe-containing LDH. Interestingly, a device for the co-delivery of adenosine as ligand and magnesium cation as ligation activator based on Mg_2Fe LDH composition showed osteogenic differentiation of stem cells as well as healing abilities when injected in tibial bone of rats [28].

The development of LDH drug carriers composed of endogenous metals such as iron is therefore of obvious interest. Iron containing LDH are also noteworthy for applications in environmental remediation [29] and energy conversion/storage [30]. All these studies have reported difficulties in the characterization of iron-based LDH due to their quite low crystallinity compared to the aluminum parent compounds and the frequent presence of impurities [31,32]. Phase segregation also tends to occur when increasing iron content resulting in the formation of hematite [33], for instance. The presence of iron may also mitigate the intercalation properties of LDH as reported for L-ascorbate into the Mg_3Fe LDH [34] and for ibuprofenate drug anions into Zn_3Al, Mg_3Al and Mg_3Fe LDH materials [35].

Phase purity is an essential feature for systems which activity will take place at molecular level, since even low amount side phases may present a biological reactivity. To the best of our knowledge, so far, only one study has addressed specifically the preparation, the thermal evolution, and the structural properties of iron containing LDH materials (Rozov et al. [36,37], for $Mg_3Fe_yAl_{(1-y)}$-CO_3 series). In the present work, both $Mg_2Fe_yAl_{(1-y)}$-Cl and $Zn_2Fe_yAl_{(1-y)}$-Cl LDH series were investigated. The M^{2+}/M^{3+} molar ratio of 2 allows a high drug loading capacity while chloride anions were chosen for their efficiency on ion exchange process and intrinsic biocompatibility [38]. Synthetic parameters were adjusted aiming to achieve both optimal purity and crystallinity. In the first part of this work, a classical approach for the characterization of the samples was

performed using X-ray diffraction (XRD), vibrational FT-IR and Raman spectroscopies, thermal and chemical elemental analysis, showing progressive changes along both series, consistent with a continuous solid solution formation in the case of Mg series and with the development of heterogeneous samples for the Zn series. In the second part, a more comprehensive analysis is proposed by combining crystal-chemical and geometrical reasoning, Rietveld refinements and pair distribution function (PDF) analysis. These approaches allowed the clear differentiation between contributions from crystalline and amorphous components, leading to a reliable determination of compositional and structural properties of both series. The use of PDF technique was decisive for the identification of 2-line ferrihydrite as an amorphous second phase in Zn series.

2. METHODS

Magnesium chloride hexahydrate ($MgCl_2 \cdot 6H_2O$) (99 %), zinc chloride ($ZnCl_2$) (≥ 99 %), aluminum chloride hexahydrate ($AlCl_3 \cdot 6H_2O$) (99 %), ferric chloride hexahydrate ($FeCl_3 \cdot 6H_2O$) (98 %), sodium hydroxide (NaOH) (≥ 98 %), D-sorbitol (> 98 %) and absolute ethanol were acquired from Sigma-Aldrich. Deionized water was obtained from a Millipore water purification system.

2.1. Synthesis of the $Mg_2Fe_yAl_{(1-y)}$-Cl and $Zn_2Fe_yAl_{(y-1)}$-Cl series.

Samples were prepared by the coprecipitation method and labelled according to the starting molar ratios used for the synthesis *i.e.* $M_2Fe_yAl_{(1-y)}$-Cl in which M is either Mg^{2+} or Zn^{2+} with a M/(Al + Fe) molar ratio that is equal to 2 and *y* corresponds to the substitution molar ratio of Al^{3+} for Fe^{3+}. Preliminary tests were performed on $Mg_2Fe_{0.5}Al_{0.5}$-Cl nominal composition to adjust the following synthesis parameters based on the work of Sun et al [39] : salts solution concentration (0.05 and 0.1 mol L^{-1}),

temperature (room temperature or 50 °C) and stirring method (magnetic at 400 rpm or mechanical stirring at 900 rpm). A Fisatom plate model 752A was employed for the magnetic stirring and a Fisatom homogenizer model 713D for the mechanical stirring. The pH value was set to 10.5 by the addition of 0.2 mol L^{-1} NaOH solution. The analyses carried out for these tests are presented and discussed in **supplementary information** (synthesis parameters in **Table S1,** XRD data in **Figure S1** and hydrodynamic particle size distribution in **Figure S2)**. The optimized conditions for the synthesis of the $Mg_2Fe_{0.5}Al_{0.5}$-Cl LDH in terms of crystallinity and apparent homogeneity were obtained for a salt solution concentration of 0.05 mol L^{-1}, a mechanical stirring at 900 rpm, and a temperature of 50°C. These conditions were then applied to all members of Mg series. They were also applied for Zn series except for the temperature, since heating may lead to the formation of $ZnO/Zn(OH)_2$ as often reported in the literature [25,40], and the pH was set to 7.5.

2.2. Characterization

X-ray diffraction (XRD) analysis for the synthesis conditions optimization tests were performed using a D8 Discover Bruker with a LYNXEYE XE-T detector, using $CuK\alpha_1$/ $K\alpha_2$ radiation (1.5406/1.5444 Å) source in Bragg Brentano θ-θ geometry, in a range between 1.5 - 70° (2θ) with scanning parameters of 0.05° steps and an 8 s count time per step. XRD data used for profile matching and structure refinement of $Mg_2Fe_yAl_{(1-y)}$-Cl and $Zn_2Fe_yAl_{(1-y)}$-Cl series were collected on a Philips X'Pert pro diffractometer equipped with a X'celerator 1D detector (2.122° active length), using $CuK\alpha_1$/ $K\alpha_2$ source in Bragg Brentano θ-θ geometry from 5 to 90°(2θ) with a scan step of 0.016°. The lattice parameters (**Table S6**) for both series were refined using the Le Bail [41] whole powder XRD pattern decomposition method with FullProf suite package [42] and assuming R-3m space group as usually reported for LDH [43]. To properly reproduce

XRD peak profile and reach good fits, it was necessary to consider microstructural effects in particular anisotropic size effects related to the platelet morphology of LDH particles. Peak broadening coming from anisotropic size effect was modelled with linear combinations of spherical harmonics as implemented in FullProf which then allowed the calculation of the volume-averaged apparent size of the coherent domains along each reciprocal lattice vector. Dimensions according to the 110 (L_{110}) and 00*l* (L_{00l}) directions are of particular interest being related to the coherence lengths within LDH hydroxide layers and along the stacking direction, respectively. LaB_6 NIST standard was used to correct for instrumental broadening.Long-range structures of $Zn_2Fe_yAl_{(1-y)}$-Cl (y = 0, 0.25, 0.5, 0.75) samples were determined via Rietveld refinement method using FullProf and details are given in the **SI**.

The atomic PDF were obtained from X-ray total scattering data collected on a PANalytical Empyrean diffractometer equipped with a solid state GaliPIX3D detector, a focusing X-ray multilayer mirror, and an Ag anticathode ($K\alpha_1$ = 0.5594214 Å, $K\alpha_2$ = 0.5638120 Å). Powder samples were placed in glass capillaries of 0.7 mm diameter. An empty capillary of the same type was measured in the same way for background subtraction. Data were recorded over the 1-145° 2θ range, which corresponds to an accessible maximum value for the scattering vector Q max of 21.4 $Å^{-1}$. Data merging, background subtraction, and $K\alpha_2$ stripping were done using HighScore Plus software provided by PANalytical Corporation. It was also used to generate a corrected and normalized total scattering structure functions S(Q) and considering the bulk chemical compositions given in **Table S2.** Finally, the PDF or G(r) were calculated from the Fourier transforms of S(Q) truncated at 21 $Å^{-1}$. The simulated PDF for 3R and 1M model structures for Zn_2Al-Cl LDH composition were calculated using PDFgui software [44].

Thermogravimetric analysis coupled to mass spectrometry (TGA-MS) was performed on a Netzsch thermoanalyser model TGA/DSC 490 PC Luxx coupled to an Aëolos 403 C mass spectrometer, using alumina crucibles with a heating rate of 10 °C min^{-1} from room temperature until 1000 °C and under a synthetic air flow of 50 mL min^{-1}.

A Jeol JSM 6610LV equipment was used for imaging $Mg_2Fe_yAl_{(1-y)}$-Cl and $Zn_2Fe_yAl_{(1-y)}$-Cl sample series (**Figure S7**) after gold sputter coating.

Quantitative analysis of Mg, Zn, Al, and Fe elements was performed by inductively coupled plasma optical emission spectroscopy (ICP-OES) with Arcos model Spectro Analytical equipment at the *Central Analítica* of *Instituto de Química* (*Universidade de São Paulo* - USP). Sampling was executed in duplicate and the analytical error is assumed to be ± 2 %. Approximately 10 mg of solid sample was dissolved with 2 mL of boiling concentrated HNO_3 until complete dissolution. Translucent solutions then were transferred to 100 mL volumetric flasks and the volume was adjusted with deionized water.

Fourier transform infrared (FT-IR) spectra of powdered samples were recorded on a Bruker spectrophotometer, model Alpha, in attenuated total reflectance (ATR) mode with a resolution of 4 cm^{-1} and 512 scans in the 4000–400 cm^{-1} range. Raman spectra were recorded at –100 ° C on a Renishaw inVia spectrometer coupled with a Leica optical microscope (RE04) with a CCD detector, using a diode laser at 785 nm (Renishaw HPNIR785), a laser potency of 5 mW (1% of the maximum beam potency) and quintuple accumulation. Low temperature was applied to limit materials luminescence and samples decomposition. Component analysis of vibrational spectra was performed using OriginPro® 9 software by applying the Voigt function [45].

3. RESULTS

3.1. Initial inspection of $Mg_2Fe_yAl_{(1-y)}$-Cl and $Zn_2Fe_yAl_{(1-y)}$-Cl compositional series

XRD patterns of $Mg_2Fe_yAl_{(1-y)}$-Cl and $Zn_2Fe_yAl_{(1-y)}$-Cl samples are showed in **Figures 1** and **2** respectively, and they are typical of LDH materials [46]. Bragg peaks were indexed considering a hexagonal cell with R-3m space group, usually reported for powdered LDH by reference to Quintinite and Hydrotalcite crystal minerals [47]. Actually, the relatively low crystallinity of the samples does not allow to consider another crystal system such as a monoclinic cell, as reported elsewhere [48]. It may be recalled that in R-3m space group, the position of the (003) reflection is related to the interlamellar distance while the (110) reflection is related to the distance between adjacent metal cations within the hydroxide layers, and it follows that $a = 2xd_{110}$ and $c = 3xd_{003}$.

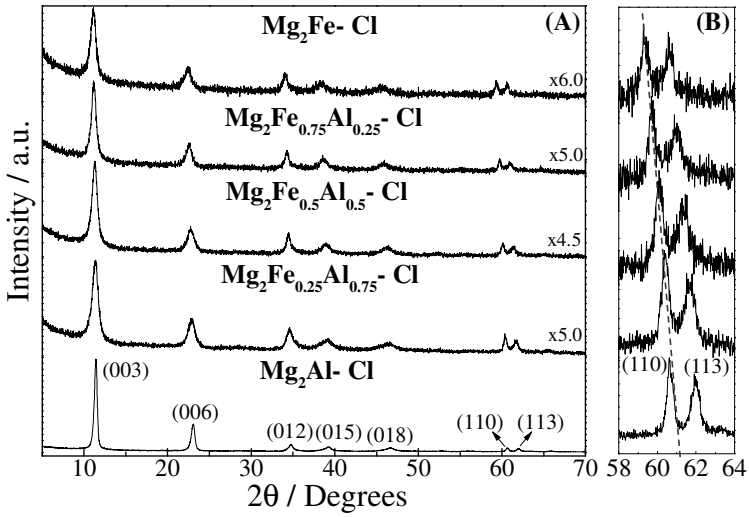

Figure 1. (A) XRD patterns of $Mg_2Fe_yAl_{(1-y)}$-Cl samples. (B) Magnification in the 58 – 64° (2θ) range (B); the dotted line shows the shift of the (110) reflection to the left as *y* increases.

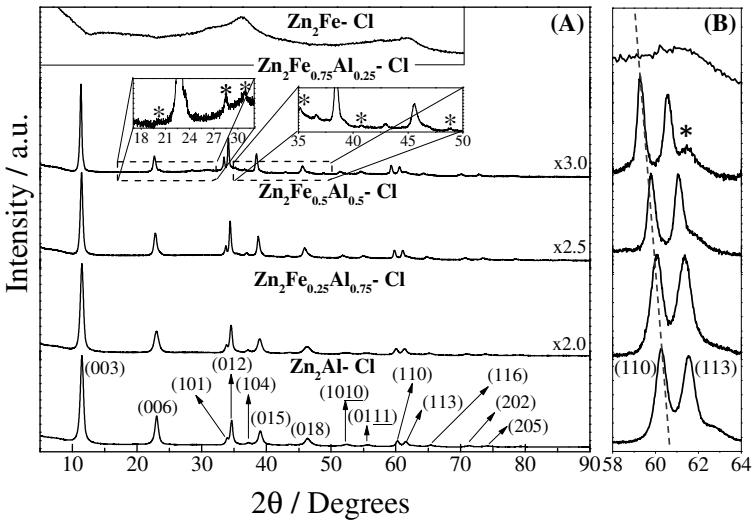

Figure 2. (A) XRD patterns of the $Zn_2Fe_yAl_{(1-y)}$-Cl samples; (*) indicates the presence of $Zn(OH)_2$ and ZnO phases. (B) Magnification in the 58 – 64 (2θ) range; the dotted line shows the shift of the (110) reflection to the left as *y* increases.

For both series, the signal to noise ratio decreases significantly between the first composition $y = 0$ and the following, which clearly indicates a decrease of the crystallinity as soon as iron is introduced into LDH layers. Mg-series appears to consist of pure LDH single phases in the whole composition range. The broadening of the Bragg peaks along this series can be related to a progressive loss of structural order and/or a decrease of the coherent domain size. For Zn series, the last composition $y = 1$ is practically amorphous with only two broad peaks observed on the XRD pattern centred at *c.a.* 35.0° and 61.2° (2θ) attributed to 2-line ferrihydrite (FH) as will be demonstrated in the second part of this study [49–51]. For $Zn_2Fe_{0.75}Al_{0.25}$-Cl sample, on can note the presence of additional low intensity peaks identified with an asterisk in **Figure 2** and attributed to the presence of $Zn(OH)_2$ and ZnO phases [52,53].

The gradual shift of the (110) reflections towards lower angles for both series (**Figures 1B** and **2B**) is consistent with the gradual incorporation of Fe^{3+} into the hydroxide layers by substitution of Al^{3+}, the ionic radii of Fe^{3+} and Al^{3+} in six-fold coordination being 0.645 and 0.535 Å [54], respectively. On the other hand, since $M^{2+}/(Al^{3+}+Fe^{3+})$ molar

ratio is constant and close to 2, the charge density of the layers does not change and therefore the interlayer content is not expected to vary, neither is the (003) reflection position.

The bulk chemical compositions of the samples and proposed LDH formulae are given in **Table S2**. For Mg series, the M^{2+}/M^{3+} molar ratios (R) measured experimentally from ICP-OES analysis are very close to the value of 2 applied during the synthesis. The presence of intercalated carbonate anions was detected by IR analysis and the quantity obtained from TGA, while remaining low (ranging from 0.05 to 0.13 per formula unit), tends to increases with *y* iron content. The amount of water molecules, also deduced from TGA, slightly increases along the series ranging from 1.5 to 2.0. On the other hand, for Zn series, except for Zn_2Al-Cl and $Zn_2Fe_{0.25}Al_{0.75}$-Cl samples, the chemical compositions of the bulk are quite different from those expected due to the value of R significantly lower than 2 and reaching a value 1.16 in the case of Zn_2Fe-Cl sample which is not consistent with the formation of LDH hydroxide layers.

The unit-cell parameters *a* and *c* for both sample series given in **Tables S3-S4** were accurately determined by full profile refinement of the XRD patterns by the Le Bail method. A linear variation of *a* cell parameter as a function of the amount of iron (*y)* experimentally measured is observed for both series as shown in **Figure 3,** which validates the existence of a continuous solid solution in the whole domain for Mg series and up to $y = 0.75$ for Zn series. The slopes of the linear regression curves being quite similar, the incorporation of iron into Mg_2Al and Zn_2Al LDH layers is indicated to proceed in the same way. This result may seem surprising in the case of Zn series given the differences in chemical compositions observed between nominal and experimental values (**Table S2**), unless it is considered that the crystallised components have a chemical composition different from the bulk and close to that expected.

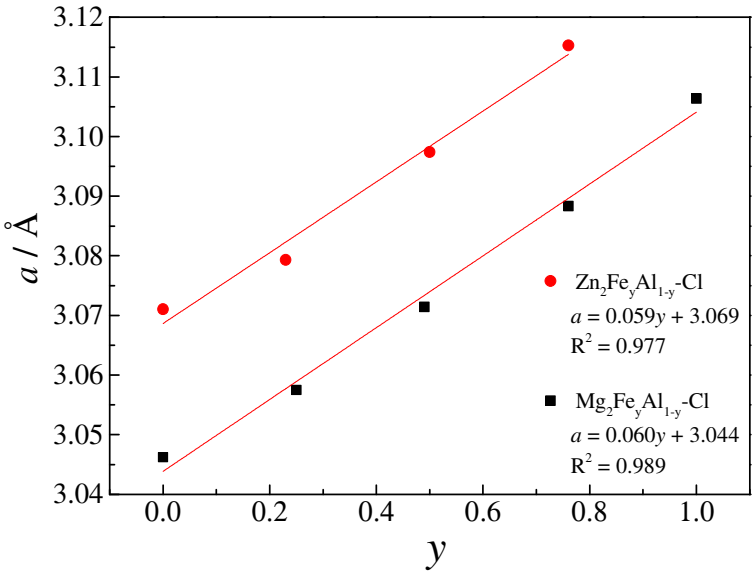

Figure 3. Variation of the lattice parameter *a* along $Mg_2Fe_yAl_{(1-y)}$-Cl and $Zn_2Fe_yAl_{(1-y)}$-Cl compositional series as a function of the amount of iron (*y)* experimentally measured.

The variation of structural and physicochemical properties along both series were also investigated by FT-IR/Raman spectroscopies and TGA. **Figure 4** shows the low frequency region of the FT-IR (1000 – 500 cm^{-1}) and Raman (600 – 200 cm^{-1}) spectra of $Mg_2Fe_yAl_{(1-y)}$-Cl and $Zn_2Fe_yAl_{(1-y)}$-Cl samples, which bands are attributed to M-OH vibration (rotatory) and M-OH translation (lattice) modes, as reported by Frost and coworkers [55–57].

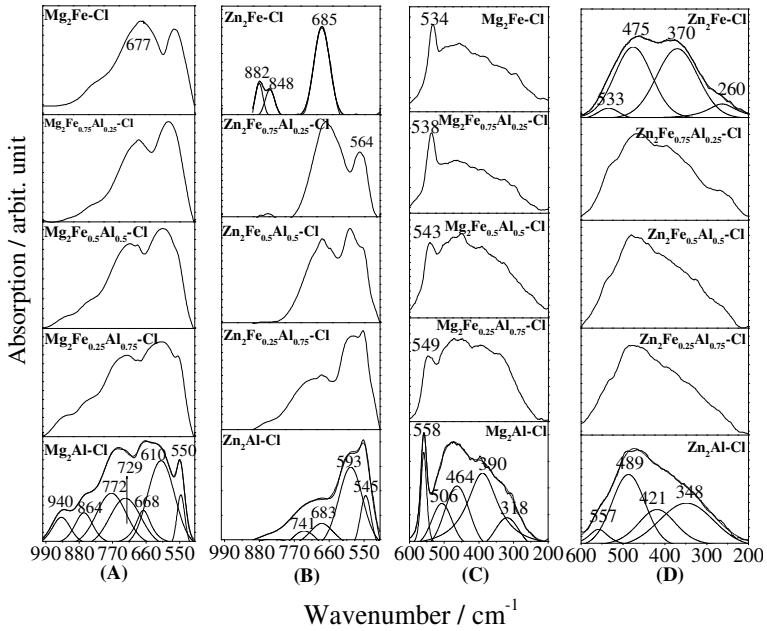

Figure 4. (A) and (B) FT-IR and (C) and (D) Raman spectra of the $Mg_2Fe_yAl_{(1-y)}$-Cl and $Zn_2Fe_yAl_{(1-y)}$-Cl samples, respectively.

For the Mg-series, the band component analysis of the IR spectrum of Mg_2Al-Cl shows bands at 550 and 772 cm^{-1} (**Figure 4A)** that can be assigned to hydroxide translation modes mainly influenced by the Al^{3+} cations (along with the corresponding deformation mode observed around 940 cm^{-1}) while the band at 610 cm^{-1} is mainly influenced by the Mg^{2+} cations. A gradual shift to lower frequency is observed for the band assigned to M^{3+}-OH, from 772 cm^{-1} for y = 0 to 677 cm^{-1} for y = 1, which is consistent with the replacement of Al^{3+} for Fe^{3+} cations due to the increase of the atomic mass of the trivalent cation. The two bands observed at 668 and 864 cm^{-1} can be attributed to the ν_4 and ν_2 modes of interlayer CO_3^{2-} anion, respectively [58]. This indicates a contamination by carbonate anions, better evidenced by the presence of the band at 1360 cm^{-1} characteristic of ν_3 mode (**Figure S5**). This contamination often takes place during the washing procedure and it is attributed to atmospheric CO_2 solubilization in water [47]. The Raman spectrum of Mg_2Al-Cl in **Figure 4C** shows a well-defined band at 558 cm^{-1} assigned to the Al-O-Al translation mode and its progressive downshift along Mg series corroborates XRD data, *i.e.* the aluminum substitution for the heavier

Fe^{3+} ion within LDH hydroxide layers. The other bands at 506, 464, 390 and 318 cm^{-1} are related to both Mg/Al-OH translations [55–57].

Similarly, the band component analysis of the FT-IR spectrum of Zn_2Al-Cl in **Figure 4B** shows bands at 545 and 741 cm^{-1} assigned to hydroxide translation modes and mainly influenced by the trivalent cation, while the band at 593 cm^{-1} is attributed to Zn-OH translation mode [59]. Due to the proximity of frequency values of these bands and also due to the appearance of impurities upon iron incorporation, the interpretation of changes along Zn series is not straightforward. The FT-IR spectrum recorded for the sample with composition $y = 1$ can be interpreted by only considering the presence of ZnO/ $Zn(OH)_2$ and FH phases. Indeed, the bands at 564 and 685 cm^{-1} are common to both Zn-based impurities and ferrihydrite, respectively, while the bands at 848 and 882 cm^{-1} can be attribute solely to ZnO/ $Zn(OH)_2$ phases [51,53,60,61]. The presence of ZnO/$Zn(OH)_2$ impurities is further confirmed at higher frequencies (**Figure S5**). The interpretation of the Raman spectra for Zn-series is not simple either (**Figure 4D)**. The shoulder observed at 557 cm^{-1} for Zn_2Al-Cl sample can be tentatively attributed to Al-OH translation mode, by similarity with Mg-series, since it is observed a redshift as the iron content increases. For the sample with composition $y = 1$, the band observed at 370 cm^{-1} may be attributed to FH [62].

The thermal analysis of the sample clearly shows a progressive decrease in the thermal stability upon iron incorporation similar to that reported for $Mg_3Fe_yAl_{(1-y)}CO_3$ [36] samples and larger for Zn series than for Mg series. These data are not presented but will be reported in a forthcoming paper.

3.2. Further insights into the structural incorporation of iron in LDH layers

For Mg series consisting of pure phases, the linear trend obtained for the variation of the cell parameter a as a function of y was further investigated based on geometrical reasoning. Indeed, it is possible to calculate the substitution ratio of divalent (x) and trivalent (y) cations in LDH from the a lattice parameter and vice versa, whichever is known with most confidence, and this can be used as a "sanity test" to validate the formation of solid solution in addition to the application of Vegard's rule [63] (**Figure 3**). The geometrical relationships in the octahedral layers of LDH were recently reviewed by Richardson [64,65] providing improved values for the effective radius of the O atom of the hydroxyl ion and a better understanding of the deformation of the metal–oxygen octahedra in the main layer. Thus, it was possible to calculate the theoretical variation of the *a* cell parameter for Mg series using the following equation:

$$a = 2\sin\frac{\alpha}{2}(r\mathrm{Mg}^{2+} + r\mathrm{OH}^{-}) - 2\sin\frac{\alpha}{2}\,(r\mathrm{Mg}^{2+} - (1-y)r\mathrm{Al}^{3+} - yr\mathrm{Fe}^{3+})x \qquad (1)$$

where x is the fraction of divalent cations, y is the fraction of Fe^{3+} cations varying from 0 to 1, α is the O-M-O bond angle within octahedra set to 97.41° for Mg-based LDH and $r\mathrm{OH}^{-}$ is the effective radius of the O atom of the hydroxyl ions with a value of 1.365 Å. The values used for the ionic radii of cations ($r\mathrm{Mg}^{2+}$, $r\mathrm{Al}^{3+}$ and $r\mathrm{Fe}^{3+}$) are those tabulated by Shannon [54]. The *a* cell parameters were determined from the full profile analysis of the XRD data and results of the refinements are given in **SI** (**Table S3** and **Figure S3**)

This theoretical variation is compared to experimental data in **Figure 7**. The solid lines represent the theoretical variation of the *a* parameter obtained from **Equation 1** against *x* for the different values of *y*. The top line corresponds to y =1, the lines below are at *y* interval of 0.25 and the last one at the bottom corresponding to y = 0. Filled squares correspond to the experimental values of the a cell parameter obtained from XRD data refinement, each associated to the experimental values of x and y determined from

chemical analysis, and are compared to crossed circles giving the expected values of the a cell parameter obtained by application of **Equation 1**.

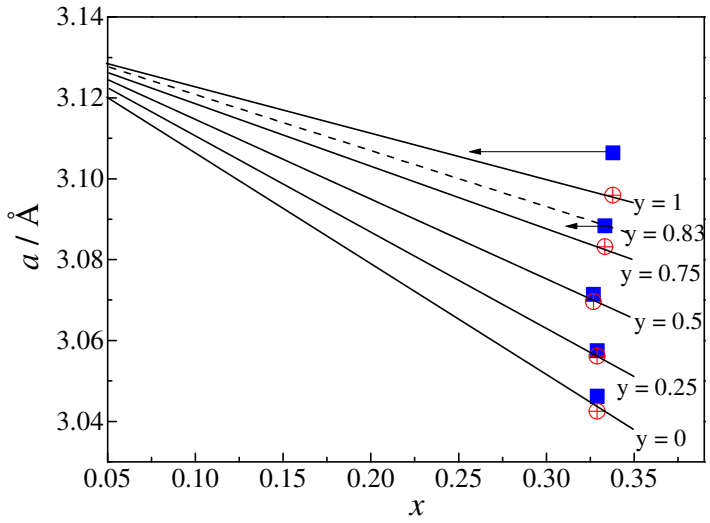

Figure 7. Crossed-analysis of XRD and chemical analysis data for the $Mg_{1-x}Fe_yAl_{(1-y)}$-Cl series: theoretical variation of the *a* lattice parameter as a function of the composition of LDH layers in terms of *x* and *y* (solid lines); experimental (filled squares) and expected (crossed circles) values of the *a* cell parameters for each experimental composition.

This crossed analysis of data can reveal composition and/or cell parameter deviations from expected values for an ideal solid solution. As can be seen, the experimental values for both a and (x,y) gradually deviate from the expected positions for $y > 0.5$. It is interesting to note that a similar deviation was observed for $Mg_3Fe_yAl_{(1-y)}$-CO_3 solid-solution series [36]. Since the cell parameters were obtained from refined Bragg peak positions, the present deviation can only be attributed to compositional errors *i.e.* a composition of LDH crystals slightly different from the bulk powder for iron rich samples. Furthermore, as XRD data for $Mg_{1-x}Fe_yAl_{(1-y)}$-Cl series do not show the presence of crystallized impurity, amorphous secondary phases must be responsible for this deviation. These compositional inconsistencies can be on the value of x or y, therefore related to Mg^{2+}/M^{3+} or Fe^{3+}/Al^{3+} molar ratios. Thus, in the case of the $Mg_2Fe_{0.75}Al_{0.25}$-Cl sample, the compositional difference between the LDH phase and the bulk would be either on *x* with a value of 0.30 instead of 0.33 as indicated by the arrow,

or on *y* with a value of 0.83 instead of 0.75 as shown by the dotted line. For Mg_2Fe-Cl sample, the difference can only be related to the value of x with a value of 0.25 instead of 0.34 leading to a Mg^{2+}/M^{3+} ratio of 3 instead of 2, in which the missing quantity of iron would still be present but in an amorphous form.

For $Zn_2Fe_yAl_{(1-y)}$-Cl series, the relative sharpness of Bragg reflections allowed a Rietveld refinement of the powder XRD data. Details are given in **SI** with refinement results in **Table S4** and **Figure S4** and refined atomic parameters in **Table S5.** As an example, the graphical output of the Rietveld refinement for the composition sample *y* = 0.5 is displayed in **Figure 8**. The main distances within the hydroxide layers and in the interlayer space are reported in **Table S6.**

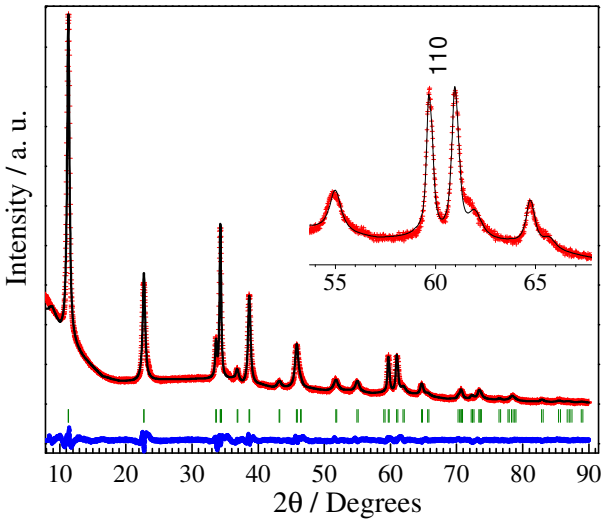

Figure 8. Graphical results of the Rietveld refinement for $Zn_2Fe_{0.5}Al_{0.5}$-Cl sample. Experimental X-ray diffraction pattern (red cross), calculated pattern (solid black line), Bragg reflections (green ticks), and difference profile (solid blue line). The inset shows the fitting of the (110) reflection from which the value of the cell parameter *a* was determined.

Correlated with the increase of the average cationic radius, it is observed a gradual increase of the *a* cell parameter as a function *y* due to the increase of the average M-OH distances across the series: 2.0232 Å for *y* = 0 *vs* 2.1148 Å for *y* = 0.75 (**Table S6**). As commonly observed in LDH structures, the $M(OH)_6$ octahedra within the hydroxide layers are distorted being flattened along the *c*-axis as indicated by OH-M-OH bond

angles significantly different from 90° and leading to two OH-OH distances, in-plane and out-of-plane distances, measured perpendicular and parallel to the c-axis respectively. These two distances increase with iron content and the increase is larger for the out of plane distance: 2.635 Å $_{\text{out of plane}}$ / 3.071 Å $_{\text{in plane}}$ for $y = 0$ *vs* 2.861 Å / 3.115 Å for $y = 1$. The OH-OH out-of-plane distance also corresponds to the thickness of the hydroxide layers; its increase results in an increase of the interlayer distance and by consequence of the *c* cell parameter. It is interesting to note that as Al^{3+} is replaced for Fe^{3+}, which ionic radius is closer to that of Zn^{2+}, the differences between the two OH-M-OH angles and also those between the two OH-OH distances are reduced so that the octahedra are less distorted: 81.26°$_{\text{out of plane}}$ / 98.74 °$_{\text{in plane}}$ for $y = 0$ *vs* 85.5°/94.50° for $y = 1$. The OH---H_2O and M---Cl/ OH---Cl distances can be used to discuss respectively the hydrogen bonding and the coulombic interactions in the interlayer space. The slight changes observed here can be attributed to the variation of the number of water molecules from one compound to another along the series and also probably to a slight variation of the charge of the layers related to M^{2+} / (Fe^{3+} + Al^{3+}) ratio. Therefore, it can be concluded that the replacement of Al or Fe into Zn_2Al LDH layers does not modify the interactions in the interlayer space and that the major effect is on the layers themselves, less distorted with more regular octahedra.

Microstructural information can also be extracted from the full profile analysis of the XRD patterns. In the present case, although stacking faults may be present, the sample contribution to the peak widths was assumed to be fully described by size-broadening effects. Using the spherical harmonic model, the coherence lengths along the [00*l*] and [110] directions could be obtained (**Table 4**), reflecting the extent of the structural order along the stacking direction (L_z) and in the plane of the hydroxide layers (L_{xy}), respectively. The formation of nanocrystals is observed with dimensions ranging from

of 8 - 34 nm. The size and shape anisotropy vary with the amount of iron and the trends are different for the two series. Differences are visible from the first compositions (y = 0). Mg_2Al-Cl nanocrystals are anisotropic in shape with L_{xy}/L_z around 1.4 consistent with a plate-like morphology typical of LDH crystals, whereas Zn_2Al-Cl displays more isotropic coherent domains with L_{xy}/L_z around 1.0 and of smaller size. Then, for $Mg_2Fe_yAl_{(1-y)}$-Cl series, the introduction of iron leads immediately to a decrease of structural coherence lengths with a value of L_z halved and then no longer changes, while L_{xy} in-plane dimension slightly re- increases. The occurrence of stacking faults, visible in the line shape of the 0*kl* reflections in the mid -2θ region of the XRD patterns (**Figures 1** and **2**), can explain the decrease of L_z dimension. On the other hand, for $Zn_2Fe_yAl_{(1-y)}$-Cl series, the structural coherence is somehow improved upon iron incorporation. The greater increase is observed for L_{xy} in-plane dimension leading to a shape anisotropy L_{xy}/L_z around 1.7 for y =0.75, and this can be explained by a reduction in the deformation of hydroxide layers built up from more regular octahedra as shown by Rietveld refinements (**Table 1**).

Table 1. Coherence lengths (Å) of crystalline domains for Mg and Zn series as determined from the modelling of XRD peak broadening by spherical harmonic functions: L_z and L_{xy} are the coherence lengths in the [00*l*] and [110] directions, respectively, also assimilated to the out-of-plane and in-plane dimensions of LDH platelets

Sample	**Coherence lengths (Å)**	***y* = 0**	**0.25**	**0.5**	**0.75**	**1**
$Mg_2Fe_yAl_{(1-y)}$-Cl	L_z	198	81	80	115	96
	L_{xy}	270	175	187	209	221
$Zn_2Fe_yAl_{(1-y)}$-Cl	L_z	119	115	150	198	-
	L_{xy}	120	133	278	339	-

SEM analyses of all samples are given in **Figure S6** showing micrometric sized platelets entangled each other, typical of LDH morphology. It should be noted that LDH particles observed by SEM are often polycrystalline secondary particles [66], as is likely the case here, resulting from the aggregation/coalescence of the primary nanoparticles as measured from peak shape analysis of XRD data. Nevertheless, the effects described

above on the primary nanoparticles for increasing amounts of iron reproduce on these secondary assemblies with a net decrease of the particle size for Mg series while maintaining the plate-like morphology, whereas for Zn series it is the reverse (except for Zn_2FeCl sample) *i.e.* a net increase of the crystallinity with platelets becoming better defined.

To link the different results together, in particular XRD data results with the bulk analysis, and better explain the deviation observed for *y* compositions above 0.5 for both series, it was performed X-ray total scattering measurements to investigate the pair distribution function. As shown by Proffen et al. [67], the PDF analysis is an interesting method to investigate systems where crystalline and amorphous structural phases co-exist. The pair distribution functions G(r) for both series for *r* values up to 200 Å are given in **Figures S7 and S8**.

The position of the peaks on the PDF reflects the distribution of distances in the materials while the intensity is proportional to the product of the scattering powers of the atoms forming the pair. Since all the contributions of all pairs of atoms are considered in the PDF, to determine to which pairs these correlations belong, it can be useful to calculate theoretical PDF starting from structural models. The experimental PDF for Zn_2Al-Cl in **Figure 9A** can be compared to the calculated PDF for 3R rhombohedral and 1M monoclinic structures in **Figure 9B**. For the 3R structure, it was applied the atomic positions obtained by Rietveld refinement for Zn_2Al-Cl sample (**Table S5**) and for the 1M structure it was considered the atomic positions reported for Quintine-1M monocristal [68]. An important aspect of PDF concerns the width of the peaks which depends on the distribution of distances for each atomic pair due to thermal displacements and static disorders [69]. In the present simulations, only individual

atomic displacement parameters as used in diffraction were considered. Details on these simulations are provided in **SI**.

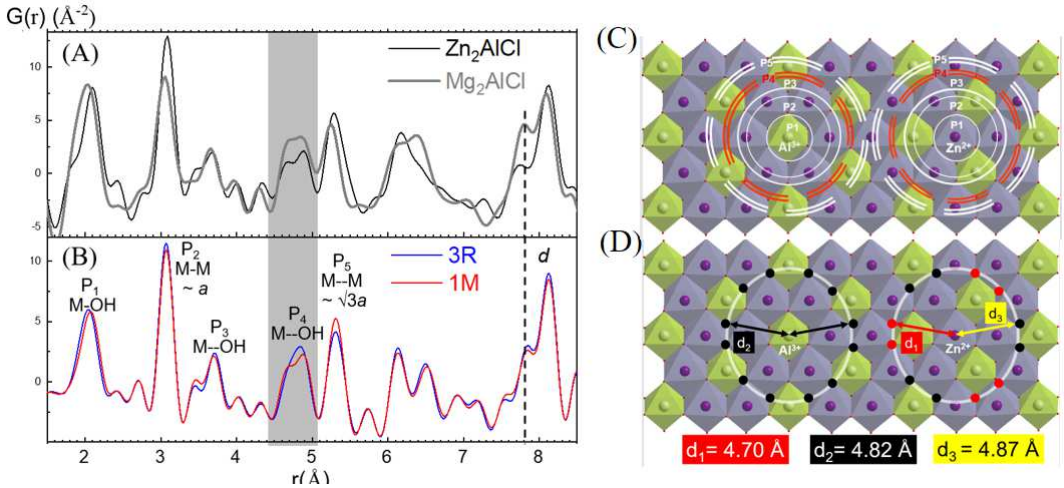

Figure 9: (A) Experimental PDF of Zn_2Al-Cl and Mg_2Al-Cl. (B) Calculated PDF for Zn_2Al-Cl composition considering either a disordered 3R rhombohedral or an ordered 1M monoclinic structure. (C) Representation of the edge-sharing octahedral layer for 1M monoclinic structure with an ordered distribution of Zn and Al cations; the contributions P1 to P5 are materialized (see text). (D) The distances pointed correspond to M---OH distances mainly contributing to P_4 peak.

From these simulations, the peaks for *r* values below the interlayer distance can be easily assigned to distances within the hydroxide layers; the contribution of the interlayer species of weaker scattering occurs only at the base of these peaks slightly modifying the intensity of the less intense peaks (**Figure S9**). Thus, the five main peaks labelled from P_1 to P_5 in **Figure 9B** are dominated by the contributions of M-OH and M-M pairs corresponding to the successive coordination shells around cations as illustrated in **Figure 9C**. The broadening of the peaks by increasing distances for the experimental data clearly indicates a statistical distribution of the distances due to structural disorder.

The main difference between rhombohedral and monoclinic structural models is the distribution of the cations within the hydroxide layer, disordered or ordered, respectively. However, this difference induces little changes on the PDF in the case of Zn_2Al hydroxide layers as can be seen in **Figure 9B** and this is probably due to the

small difference in bond length between Zn-OH and Al-OH. Only a slight modification is observed for the peak labelled P_4 at *r* around 4.8 Å dominated by M---OH contributions from the third coordination shell. As illustrated in **Figure 9D**, in case of an ordered distribution of M^{2+} and M^{3+} cations, two distinct M---OH distances (d_1 and d_3) are expected around M^{2+} and only one around M^{3+} cations (d_2) thus leading to a double peak on the PDF. Due to the difference in scattering power between Zn and Al atoms, a shoulder peak is expected and this is exactly what is observed on the experimental PDF for Zn_2Al sample, thus indicating an ordered distribution of the cations at least in local range. Indeed, the extent of this cation ordering across the layer cannot be determined owing to the greater number of contributions when increasing *r* range, within the layers and also from adjacent layers. As can be seen in **Figure 9A**, Mg_2Al-Cl sample also displays a P_4 double peak and one can also attribute it to a local order of the cations. The observation of a double instead of a shoulder peak in this latter case is certainly due to the fact that Mg^{2+} and Al^{3+} cations display similar X ray scattering powers. To the best of our knowledge, this is the first time that local cation ordering in LDH system is evidenced using PDF technique.

For Mg series, a gradual evolution of P_1 and P_2 PDF peaks is observed in **Figure 10A**. P_1 results from a single atomic pair (*i.e.* M-OH in the first nearest neighbor shell) while P_2 results from the contribution of different atomic pairs although dominated by the M---M atomic pair between first nearest neighbor cations. For $y = 0$, P_1 displays a shoulder attributed to Al-OH distances which disappears as Al^{3+} ions are replaced by Fe^{3+}; Fe-OH distances being closer to Mg-OH distances, P_1 peak width decreases. The increase of the number of Fe-OH pairs also leads to an increase of the intensity of P_1. Concomitantly and as expected, the position of P_2 which is related to the sum of the ionic radii of M cations is shifted to higher distances and can be compared to the *a* parameter of the

rhombohedral cell obtained from Bragg peak positions (**Table S3**). While similar values are obtained for $y = 0$ and 0.5, different values are observed for $MgFe_2$-Cl sample with a maximum measured at 3.09 Å for P_2 peak and a value of 3.11 Å for the *a* cell parameter. This indicates that the crystalline component as measured by XRD is not the only phase contributing to the signal measured by PDF. This result is actually consistent with chemical/XRD data crossed analysis by Richardson's method given above and suggests the probable presence of an amorphous phase for $y > 0.5$. For Mg_2Fe-Cl sample, it is also noted the presence of an additional peak on the PDF at 3.45 Å that could be attributed to the presence of iron hydroxide species as shown below.

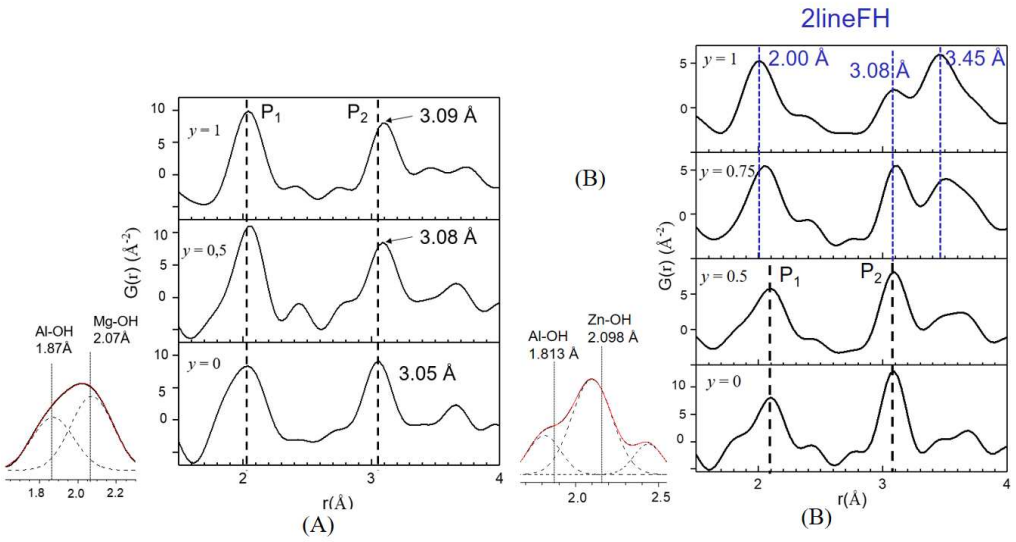

Figure 10. Expanded view of PDFs in the range 1-4 Å for (A) $Mg_2Fe_yAl_{(1-y)}$-Cl series and (B) $Zn_2Fe_yAl_{(1-y)}$-Cl series. The black dotted lines are anchored to the composition $y = 0$. The blue dotted lines indicate the PDF peaks of 2-line FH. On the left of each Figures is given the Gaussian fit of P_1 peak for $y = 0$ composition samples.

On the other hand, changes are more difficult to be observed for Zn series due to the presence of FH, which occurs probably from $y = 0.5$ and is the major phase for $y = 1$ (**Figure 10B**). FH is a nano Fe^{3+} oxide material widely present in nature which structure has not been clearly established yet [70]. PDF data profile measured for the Zn_2Fe-Cl sample is very similar to the PDF data reported for 2-line FH by Tang et al. [71]. In FH, iron is both tetrahedrally and octahedrally coordinated; the first peak in the PDF at

around 2.0 Å is attributed to Fe-O pairs while the peaks at around 3.03 Å and 3.40 Å are mainly ascribed to Fe-Fe correlations between adjacent FeO_6 octahedra linked in edge-sharing and corner-sharing configurations, respectively. To the best of our knowledge, this is the first time that FH impurity is so clearly identified in iron containing LDH.

4. DISCUSSION

Iron-containing LDH phases have recently attracted much interests in several application fields, in particular in the medical field [1,10]. However, most of the studies reported so far suffers from insufficient data concerning the conditions of formation and the determination of the fine chemical composition of Fe-LDH which can hinder the development of applications. Mention should be made of the studies carried out by Rozov et al. [36,37] who examined in detail the composition, structure, solubility, and thermodynamic properties of $[Mg_3Fe_yAl_{(1-y)}(OH)_8](CO_3)_{0.5}\cdot 2.5H_2O$ hydrotalcite - pyroaurite solid solutions with $Mg^{2+}/(Al^{3+} + Fe^{3+})$ mole ratio (R) equal to 3. The other studies are mainly focused on applications and the chemical analysis of the materials is often not provided. In the case of Zn_RFe phases, the results appear very disparate. The studies mostly concern compositions with Zn/Fe molar ratios close to 3 and show poorly crystalline materials [25,40] often containing impurities not always identified but recognized here as ZnO and/or ferrihydrite [72–74]. Furthermore, the lack of comparative analysis of the bulk and crystalline components clearly leads to inconsistencies in the chemical compositions provided [75].

The present study aims to develop iron-rich LDH phases, *i.e.* with a R value equal to 2. The gradual incorporation of iron into Mg_2Al-Cl and Zn_2Al-Cl LDH in substitution of aluminum was examined in detail considering both compositional and structural aspects. First, preliminary characterization using conventional techniques including

powder X-ray diffraction, IR and Raman spectroscopies, ICP elemental analysis, and TGA analyses clearly shows two different behaviors. A complete series of $Mg_2Fe_yAl_{(1-y)}$-Cl LDH compositions could be synthetized between the Al and Fe end members and such results suggested that this series may represent a continuous solid solution. On the other hand, for $Zn_2Fe_yAl_{(1-y)}$-Cl compounds, iron incorporation was observed only up to $y = 0.75$ (nominal value) with the presence of $Zn(OH)_2$/ZnO impurities for $y \geq 0.5$ and the bulk chemical compositions are different from those expected.

From these preliminary results, it is clear that further thorough examination was required from both compositional and structural point of views to better understand differences between $Mg_2Fe_yAl_{(1-y)}$-Cl and $Zn_2Fe_yAl_{(1-y)}$-Cl series. For Mg series, the crystal-chemical plausibility of the solid solution was checked as proposed by Richardson [64,65]. By combining XRD and chemical analysis data sets, it was possible to show that for $y \geq 0.5$ the composition of LDH crystalline phase actually deviates from that expected by only replacing Al by Fe and is different from that of the bulk. Chemical analysis of the bulk for Mg_2Fe-Cl sample indicates a value of R equal to 2, nearly equal to the synthesis conditions, while geometrical reasoning applied on the crystalline component gives a value of 3, thus indicating the presence of an iron rich, amorphous and undetected second phase. Interestingly, the same data treatment performed for $[Mg_3Fe_yAl_{(1-y)}(OH)_8](CO_3)_{0.5}\cdot 2.5H_2O$ hydrotalcite-pyroaurite data also reveal a deviation from ideality for $y \geq 0.6$ due to an increase of the R value [36].

In the case of Zn series, for y values higher than 0.5, the presence of 2-line ferrihydrite FH was clearly demonstrated by PDF analysis. Although it has never been indicated as a probable secondary phase in the synthesis of Fe-LDH so far, its occurrence is not surprising. Indeed, 2-line FH is reported to be instantaneously formed from the Fe^{3+} ion hydrolysis [76,77]. Considering the solubility product of the isolated metallic

hydroxides (Fe^{3+} < Al^{3+} < Zn^{2+} < Mg^{2+}) [78], Fe^{3+}-oxyhydroxide phases are easily precipitated. Furthermore, although thermodynamically unstable due to its low structural organization, 2-line FH transformation is inhibited in the presence of Zn cations [79]. FH can even act as a precursor for the formation of zinc hydroxides phases [80–82] and subsequent transformation into ZnO [83–85]. Finally, FH shows a solubility minimum at pH 7-8 which is consistent with the pH applied here for the synthesis of the Zn-series, *i.e.* 7.5. It has been established for LDH phases composed of only one type of divalent and trivalent cations that their stability are higher compared to single hydroxide phases, also that Al-containing LDH phase formation is more spontaneous than Fe- LDH [36,86]. However, these trends may not necessarily apply to the preparation of multi metallic LDH with more than one type of divalent/trivalent cations. As shown here for $Zn_2Fe_yAl_{(1-y)}$ composition, at pH 7.5, when the iron content exceeds the aluminum content ($y \geq 0.5$), the precipitation of iron in FH form is found to prevail preventing the formation of LDH layer. Comparatively, Mg series was prepared at pH 10.5 for which FH solubility is higher [77]. Therefore, it would be expected that the increase in synthetic pH could be an alternative for preparing the Zn_2Fe-Cl composition. However, by slightly increasing the pH to 8.5, $Zn(OH)_2$/ZnO phases are formed as shown by XRD (**Figure S1B**).

The present study also attempted to gain insights into the structural and microstructural modifications accompanying iron incorporation. For the first time, using the PDF technique, it was possible to detect a local ordered distribution of the cations in the Mg_2Al and Zn_2Al LDH layers which disappears as soon as iron is present. The resulting loss of crystallinity was quantified from Bragg peaks broadening analysis and the determination of the size of the coherent domains. For $y \geq 0,5$, both systems tend to regain crystallinity, probably because the ionic radius of Fe^{3+} is closer to the ionic radius

of Zn^{2+} or Mg^{2+} divalent cation than is Al^{3+}. The Rietveld analysis of LDH crystalline component for Zn-series shows that $Zn_2Fe_yAl_{(1-y)}$ hydroxide layers consist of more and more regular octahedra as Al^{3+} is replaced by Fe^{3+}.

CONCLUSIONS

This study provides useful elements for better understanding and interpreting the results reported in the literature regarding iron-containing LDH phases. It is recalled that for a complete compositional and structural characterization of LDH, it is essential to differentiate the bulk to the crystalline component in order to identify possible contributions from amorphous components. In this sense, as shown here, PDF technique can be useful to link these different contributions together. It is shown that $Mg_2Fe_yAl_{(1-y)}$-Cl solids with $y \leq 0.5$ can be obtained as pure phases with a fine control of their compositions, as requested for pharmaceutical formulations.

Supporting Information

Details concerning the optimization of the synthesis of LDH; chemical composition; Le Bail and Rietveld refinements of X-ray diffraction data; FT-IR spectra in the 4000-400 cm^{-1} range; SEM micrographs; additional PDF results.

AUTHORS INFORMATION

Corresponding Authors

*corresponding authors: Christine Taviot-Guého, christine.taviot-gueho@uca.fr

Authors Contributions

Mariana Pires Figueiredo: investigation, data curation, visualization, and writing - original draft. **Alfredo Duarte** and **Victor Vendruscolo:** investigation, writing - review & editing. **Rodolphe Thirouard:** investigation. **Vera R. L. Constantino:** writing -

review & editing, validation, supervision, and funding acquisition. **Christine Taviot-Guého:** conceptualization, methodology, formal analysis, visualization, writing the original draft. All authors have reviewed and given approval to the final version of the manuscript.

Funding Sources

This work was supported by Fundação de Amparo à Pesquisa do Estado de São Paulo (FAPESP 2016/13862-9, scholarship to M.P.F.), Conselho Nacional de Desenvolvimento Científico e Tecnológico (CNPq 305446/2017-7, research grant to V.R.L.C.) and Research Academic Cooperation Agreement CNRS/FAPESP (PRC project 1688 and SPRINT 2016/50317-9).

Notes

The authors declare don't have known competing financial interests or conflicting interests.

ACKNOWLEDGEMENTS

The authors are grateful to the Laboratório de Espectroscopia Molecular Hans Stammreich (Instituto de Química – USP) for the FT-IR spectra recording, to the Laboratório de Astrobiologia (Instituto de Química – USP) for the Raman spectra recording, to the Laboratório de Materiais Híbridos (Instituto de Ciências Ambientais, Químicas e Farmacêuticas – UNIFESP) for the SEM micrographs recording and also to the Laboratório de Cristalografia (Instituto de Física – USP) for the XRD patterns recording in the D8 Discover Bruker equipment.

REFERENCES

[1] G. Mishra, B. Dash, S. Pandey, Layered double hydroxides: A brief review from fundamentals to application as evolving biomaterials, Applied Clay Science. 153 (2018) 172–186. https://doi.org/10.1016/j.clay.2017.12.021.

[2] C. Prasad, H. Tang, Q.Q. Liu, S. Zulfiqar, S. Shah, I. Bahadur, An overview of semiconductors/layered double hydroxides composites: Properties, synthesis,

photocatalytic and photoelectrochemical applications, Journal of Molecular Liquids. 289 (2019) 111114. https://doi.org/10.1016/j.molliq.2019.111114.

[3] Y. Zhao, X. Jia, G.I.N. Waterhouse, L.-Z. Wu, C.-H. Tung, D. O'Hare, T. Zhang, Layered Double Hydroxide Nanostructured Photocatalysts for Renewable Energy Production, Advanced Energy Materials. 6 (2016) 1501974. https://doi.org/10.1002/aenm.201501974.

[4] C.-W. Jeon, S.-S. Lee, I.-K. Park, Flexible Visible-Blind Ultraviolet Photodetectors Based on ZnAl-Layered Double Hydroxide Nanosheet Scroll, ACS Appl. Mater. Interfaces. 11 (2019) 35138–35145. https://doi.org/10.1021/acsami.9b12082.

[5] M. Zubair, M. Daud, G. McKay, F. Shehzad, M.A. Al-Harthi, Recent progress in layered double hydroxides (LDH)-containing hybrids as adsorbents for water remediation, Applied Clay Science. 143 (2017) 279–292. https://doi.org/10.1016/j.clay.2017.04.002.

[6] V. Rives, M. del Arco, C. Martín, Layered double hydroxides as drug carriers and for controlled release of non-steroidal antiinflammatory drugs (NSAIDs): A review, Journal of Controlled Release. 169 (2013) 28–39. https://doi.org/10.1016/j.jconrel.2013.03.034.

[7] L. Li, W. Gu, J. Chen, W. Chen, Z.P. Xu, Co-delivery of siRNAs and anti-cancer drugs using layered double hydroxide nanoparticles, Biomaterials. 35 (2014) 3331–3339. https://doi.org/10.1016/j.biomaterials.2013.12.095.

[8] H. Nakayama, N. Wada, M. Tsuhako, Intercalation of amino acids and peptides into Mg-Al layered double hydroxide by reconstruction method, Int J Pharm. 269 (2004) 469–478. https://doi.org/10.1016/j.ijpharm.2003.09.043.

[9] Z.P. Xu, T.L. Walker, K. Liu, H.M. Cooper, G.Q.M. Lu, P.F. Bartlett, Layered double hydroxide nanoparticles as cellular delivery vectors of supercoiled plasmid DNA, Int J Nanomedicine. 2 (2007) 163–174. https://pubmed.ncbi.nlm.nih.gov/17722544.

[10] A. Vaccari, Layered double hydroxides: present and future: V. Rives (Ed.), Nova Science Publishers, Inc., New York, 2001, IX+439 pp., ISBN 1-59033-060-9, Applied Clay Science. 22 (2002) 75–76. https://doi.org/10.1016/S0169-1317(02)00112-6.

[11] K. Klotz, W. Weistenhöfer, F. Neff, A. Hartwig, C. van Thriel, H. Drexler, The Health Effects of Aluminum Exposure, Deutsches Aerzteblatt Online. (2017). https://doi.org/10.3238/arztebl.2017.0653.

[12] C.L. Peterson, D.L. Perry, H. Masood, J.L. White, S.L. Hem, C. Fritsch, F. Haeusler, Characterization of Antacid Compounds Containing Both Aluminum and Magnesium. II. Codried Powders, Pharmaceutical Research. 10 (1993) 1005–1007. https://doi.org/10.1023/A:1018910705853.

[13] A.S. Tarnawski, M. Tomikawa, M. Ohta, I.J. Sarfeh, Antacid talcid activates in gastric mucosa genes encoding for EGF and its receptor. The molecular basis for its ulcer healing action, Journal of Physiology-Paris. 94 (2000) 93–98. https://doi.org/10.1016/S0928-4257(00)00149-2.

[14] A. Schmassmann, A. Tarnawski, H.A. Gerber, B. Flogerzi, M. Sanner, L. Varga, F. Halter, Antacid provides better restoration of glandular structures within the gastric ulcer scar than omeprazole, Gut. 35 (1994) 896–904. https://doi.org/10.1136/gut.35.7.896.

[15] E. Wölke, M. Seiberling, C. Schepers, U. Roos, H. Franke, I. Bernhard, Investigation in healthy volunteers to evaluate serum concentrations and urinary excretions of aluminium, magnesium, calcium and phosphate after multiple administration of hydrotalcit (Talcid®) suspension, Bollettino Chimico Farmaceutico. 132 (1993) 234–40.

[16] M. Mold, E. Shardlow, C. Exley, Insight into the cellular fate and toxicity of aluminium adjuvants used in clinically approved human vaccinations, Sci Rep. 6 (2016) 31578. https://doi.org/10.1038/srep31578.

[17] V.R.R. Cunha, V.A. Guilherme, E. de Paula, D.R. de Araujo, R.O. Silva, J.V.R. Medeiros, J.R.S.A. Leite, P.A.D. Petersen, M. Foldvari, H.M. Petrilli, V.R.L. Constantino, Delivery system for mefenamic acid based on the nanocarrier layered double hydroxide: Physicochemical characterization and evaluation of anti-inflammatory and

antinociceptive potential, Materials Science and Engineering: C. 58 (2016) 629–638. https://doi.org/10.1016/j.msec.2015.08.037.

[18] Y. Kuthati, R.K. Kankala, C.-H. Lee, Layered double hydroxide nanoparticles for biomedical applications: Current status and recent prospects, Applied Clay Science. 112–113 (2015) 100–116. https://doi.org/10.1016/j.clay.2015.04.018.

[19] V. Kumar, K. Gill, Aluminium neurotoxicity: Neurobehavioural and oxidative aspects, Archives of Toxicology. 83 (2009) 965–978. https://doi.org/10.1007/s00204-009-0455-6.

[20] M.P. Figueiredo, V.R.R. Cunha, F. Leroux, C.T. Gueho, M.N. Nakamae, Y.R. Kang, R.B. Souza, A.M.C.R.P.F. Martins, I.H.J. Koh, V.R.L. Constantino, Iron-based layered double hydroxide implants: potential drug delivery carriers with tissue biointegration promotion and blood microcirculation preservation, Acs Omega. 3 (2018) 18263–18274.

[21] Q. Li, D. Wang, J. Qiu, F. Peng, X. Liu, Regulating the local pH level of titanium: Via Mg-Fe layered double hydroxides films for enhanced osteogenesis, Biomaterials Science. 6 (2018). https://doi.org/10.1039/C8BM00100F.

[22] Y.-F. Lung, Y.-S. Sun, C.-K. Lin, J.-Y. Uan, H.-H. Huang, Synthesis of Mg-Fe-Cl hydrotalcite-like nanoplatelets as an oral phosphate binder: evaluations of phosphorus intercalation activity and cellular cytotoxicity, Sci Rep. 6 (2016) 32458. https://doi.org/10.1038/srep32458.

[23] Y. Ding, L. Liu, Y. Fang, X. Zhang, M. Lyu, S. Wang, The Adsorption of Dextranase onto Mg/Fe-Layered Double Hydroxide: Insight into the Immobilization, Nanomaterials. 8 (2018) 173. https://doi.org/10.3390/nano8030173.

[24] 2018 Li Regulating the local pH level of titanium via Mg-Fe layered double.pdf, (n.d.).

[25] F. Peng, D. Wang, D. Zhang, H. Cao, X. Liu, The prospect of layered double hydroxide as bone implants: A study of mechanical properties, cytocompatibility and antibacterial activity, Applied Clay Science. 165 (2018) 179–187. https://doi.org/10.1016/j.clay.2018.08.020.

[26] A. Weizbauer, M. Kieke, M.I. Rahim, G.L. Angrisani, E. Willbold, J. Diekmann, T. Flörkemeier, H. Windhagen, P.P. Müller, P. Behrens, S. Budde, Magnesium-containing layered double hydroxides as orthopaedic implant coating materials-An *in vitro* and *in vivo* study: LDH AS POTENTIAL ORTHOPAEDIC IMPLANT COATING MATERIALS, J. Biomed. Mater. Res. 104 (2016) 525–531. https://doi.org/10.1002/jbm.b.33422.

[27] B. Balcomb, M. Singh, S. Singh, Synthesis and Characterization of Layered Double Hydroxides and Their Potential as Nonviral Gene Delivery Vehicles, ChemistryOpen. 4 (2015) 137–145. https://doi.org/10.1002/open.201402074.

[28] H. Kang, M. Kim, Q. Feng, S. Lin, K. Wei, R. Li, C.J. Choi, T.-H. Kim, G. Li, J.-M. Oh, L. Bian, Nanolayered hybrid mediates synergistic co-delivery of ligand and ligation activator for inducing stem cell differentiation and tissue healing, Biomaterials. 149 (2017) 12–28. https://doi.org/10.1016/j.biomaterials.2017.09.035.

[29] Z. Yang, C. Zhang, G. Zeng, X. Tan, H. Wang, D. Huang, K. Yang, J. Wei, C. Ma, K. Nie, Design and engineering of layered double hydroxide based catalysts for water depollution by advanced oxidation processes: a review, J. Mater. Chem. A. 8 (2020) 4141–4173. https://doi.org/10.1039/C9TA13522G.

[30] R. Patel, J.T. Park, M. Patel, J.K. Dash, E.B. Gowd, R. Karpoormath, A. Mishra, J. Kwak, J.H. Kim, Transition-metal-based layered double hydroxides tailored for energy conversion and storage, J. Mater. Chem. A. 6 (2018) 12–29. https://doi.org/10.1039/C7TA09370E.

[31] M. Pigna, J.J. Dynes, A. Violante, A. Sommella, A.G. Caporale, Sorption of Arsenite on Cu-Al, Mg-Al, Mg-Fe, and Zn-Al Layered Double Hydroxides in the Presence of Inorganic Anions Commonly Found in Aquatic Environments, Environmental Engineering Science. 33 (2016) 98–104. https://doi.org/10.1089/ees.2015.0131.

[32] E.M. Seftel, P. Cool, D. Lutic, Mg–Al and Zn–Fe layered double hydroxides used for organic species storage and controlled release, Materials Science and Engineering: C. 33 (2013) 5071–5078. https://doi.org/10.1016/j.msec.2013.08.041.

[33] K. Morimoto, K. Tamura, H. Yamada, T. Sato, M. Suzuki, Determination and reduction of Fe(III) incorporated into Mg–Fe layered double hydroxide structures, Applied Clay Science. 121–122 (2016) 71–76. https://doi.org/10.1016/j.clay.2015.12.008.

[34] X. Gao, L. Lei, D. O'Hare, J. Xie, P. Gao, T. Chang, Intercalation and controlled release properties of vitamin C intercalated layered double hydroxide, Journal of Solid State Chemistry. 203 (2013) 174–180. https://doi.org/10.1016/j.jssc.2013.04.028.

[35] P. Ding, S.F. Tang, Z.Z. Li, Influence of Metal Cations on the Structure and Release Property of Layered Double Hydroxide-Ibuprofen Host-Guest Materials, AMR. 152–153 (2010) 556–559. https://doi.org/10.4028/www.scientific.net/AMR.152-153.556.

[36] K. Rozov, U. Berner, C. Taviot-Gueho, F. Leroux, G. Renaudin, D. Kulik, L.W. Diamond, Synthesis and characterization of the LDH hydrotalcite–pyroaurite solid-solution series, Cement and Concrete Research. 40 (2010) 1248–1254. https://doi.org/10.1016/j.cemconres.2009.08.031.

[37] K.B. Rozov, U. Berner, D.A. Kulik, L.W. Diamond, Solubility and Thermodynamic Properties of Carbonate-Bearing Hydrotalcite—Pyroaurite Solid Solutions with A 3:1 Mg/(Al+Fe) Mole Ratio, Clays and Clay Minerals. 59 (2011) 215–232. https://doi.org/10.1346/CCMN.2011.0590301.

[38] S.-J. Choi, J.-H. Choy, Effect of physico-chemical parameters on the toxicity of inorganic nanoparticles, J. Mater. Chem. 21 (2011) 5547. https://doi.org/10.1039/c1jm10167f.

[39] X. Sun, E. Neuperger, S.K. Dey, Insights into the synthesis of layered double hydroxide (LDH) nanoparticles: Part 1. Optimization and controlled synthesis of chloride-intercalated LDH, Journal of Colloid and Interface Science. 459 (2015) 264–272. https://doi.org/10.1016/j.jcis.2015.07.073.

[40] S.A.A. Moaty, A.A. Farghali, R. Khaled, Preparation, characterization and antimicrobial applications of Zn-Fe LDH against MRSA, Materials Science and Engineering: C. 68 (2016) 184–193. https://doi.org/10.1016/j.msec.2016.05.110.

[41] A.L. Bail, H. Duroy, J.L. Fourquet, Ab-initio structure determination of LiSbWO6 by X-ray powder diffraction, Materials Research Bulletin. 23 (1988) 447–452. https://doi.org/10.1016/0025-5408(88)90019-0.

[42] J. Rodriguez-Carvajal, Recent developments of the program FULLPROF, commission on powder diffraction, IUCr Newsl. 26 (2001).

[43] D.G. Evans, R.C.T. Slade, Structural Aspects of Layered Double Hydroxides, in: Springer-Verlag, Berlin/Heidelberg, 2005. https://doi.org/10.1007/430_005.

[44] C. Farrow, P. Juhas, J. Liu, D. Bryndin, E. Bozin, J. Bloch, T. Proffen, S. Billinge, PDFfit2 and PDFgui: Computer Programs for Studying Nanostructure in Crystals, Journal of Physics. Condensed Matter : An Institute of Physics Journal. 19 (2007) 335219. https://doi.org/10.1088/0953-8984/19/33/335219.

[45] R. Meier, On art and science in curve-fitting vibrational spectra, Vibrational Spectroscopy - VIB SPECTROSC. 39 (2005) 266–269. https://doi.org/10.1016/j.vibspec.2005.03.003.

[46] C. Forano, T. Hibino, F. Leroux, C. Taviot-Guého, Chapter 13.1 Layered Double Hydroxides, in: Developments in Clay Science, Elsevier, 2006: pp. 1021–1095. https://doi.org/10.1016/S1572-4352(05)01039-1.

[47] E. Conterosito, L. Palin, D. Antonioli, D. Viterbo, E. Mugnaioli, U. Kolb, L. Perioli, M. Milanesio, V. Gianotti, Structural Characterisation of Complex Layered Double Hydroxides and TGA-GC-MS Study on Thermal Response and Carbonate Contamination in Nitrate- and Organic-Exchanged Hydrotalcites, Chem. Eur. J. 21 (2015) 14975–14986. https://doi.org/10.1002/chem.201500450.

[48] K. Jayanthi, P.V. Kamath, A Crystal Chemical Approach to a Cation-Ordered Structure Model for Carbonate-Intercalated Layered Double Hydroxides, Crystal Growth & Design. 16 (2016) 4450–4456. https://doi.org/10.1021/acs.cgd.6b00562.

[49] S. Das, M.J. Hendry, J. Essilfie-Dughan, Transformation of Two-Line Ferrihydrite to Goethite and Hematite as a Function of pH and Temperature, Environ. Sci. Technol. 45 (2011) 268–275. https://doi.org/10.1021/es101903y.

[50] F. Frau, D. Addari, A. Davide, R. Biddau, R. Cidu, A. Rossi, Influence of Major Anions on As(V) Adsorption by Synthetic 2-line Ferrihydrite. Kinetic Investigation and XPS Study of the Competitive Effect of Bicarbonate, Water, Air, and Soil Pollution. 205 (2009) 25–41. https://doi.org/10.1007/s11270-009-0054-4.

[51] M. Ristić, E. De Grave, S. Musić, S. Popović, Z. Orehovec, Transformation of low crystalline ferrihydrite to α-Fe2O3 in the solid state, Journal of Molecular Structure. 834–836 (2007) 454–460. https://doi.org/10.1016/j.molstruc.2006.10.016.

[52] M. Wang, Y. Zhou, Y. Zhang, S.H. Hahn, E.J. Kim, From Zn(OH)2 to ZnO: a study on the mechanism of phase transformation, CrystEngComm. 13 (2011) 6024. https://doi.org/10.1039/c1ce05502j.

[53] D.A. Giannakoudakis, J.A. Arcibar-Orozco, T.J. Bandosz, Key role of terminal hydroxyl groups and visible light in the reactive adsorption/catalytic conversion of mustard gas surrogate on zinc (hydr)oxides, Applied Catalysis B: Environmental. 174–175 (2015) 96–104. https://doi.org/10.1016/j.apcatb.2015.02.028.

[54] R.D. Shannon, Revised effective ionic radii and systematic studies of interatomic distances in halides and chalcogenides, Acta Cryst A. 32 (1976) 751–767. https://doi.org/10.1107/S0567739476001551.

[55] J.T. Kloprogge, L. Hickey, R.L. Frost, FT-Raman and FT-IR spectroscopic study of synthetic Mg/Zn/Al-hydrotalcites, J. Raman Spectrosc. 35 (2004) 967–974. https://doi.org/10.1002/jrs.1244.

[56] J.T. Kloprogge, R.L. Frost, Fourier Transform Infrared and Raman Spectroscopic Study of the Local Structure of Mg-, Ni-, and Co-Hydrotalcites, Journal of Solid State Chemistry. 146 (1999) 506–515. https://doi.org/10.1006/jssc.1999.8413.

[57] S.J. Palmer, R.L. Frost, H.J. Spratt, Synthesis and Raman spectroscopic study of Mg/Al,Fe hydrotalcites with variable cationic ratios, J. Raman Spectrosc. 40 (2009) 1138–1143. https://doi.org/10.1002/jrs.2198.

[58] Kazuo Nakamoto, Infrared and Raman Spectra of Inorganic and Coordination Compounds, Part A: Theory and Applications in Inorganic Chemistry, 6th ed., WILEY, 2009.

[59] E.M. Seftel, E. Popovici, M. Mertens, P. Cool, E.F. Vansant, Infrared and Raman spectroscopic study of Sn-containing Zn/Al-layered double hydroxides, (n.d.) 6.

[60] R.C. Pereira, P.R. Anizelli, E. Di Mauro, D.F. Valezi, A.C.S. da Costa, C.T.B.V. Zaia, D.A.M. Zaia, The effect of pH and ionic strength on the adsorption of glyphosate onto ferrihydrite, Geochem Trans. 20 (2019) 3. https://doi.org/10.1186/s12932-019-0063-1.

[61] W. Xiao, A.M. Jones, R.N. Collins, M.W. Bligh, T.D. Waite, Use of fourier transform infrared spectroscopy to examine the Fe(II)-Catalyzed transformation of ferrihydrite, Talanta. 175 (2017) 30–37. https://doi.org/10.1016/j.talanta.2017.07.018.

[62] L. Mazzetti, P.J. Thistlethwaite, Raman spectra and thermal transformations of ferrihydrite and schwertmannite, J. Raman Spectrosc. 33 (2002) 104–111. https://doi.org/10.1002/jrs.830.

[63] L. Vegard, Die Konstitution der Mischkristalle und die Raumfüllung der Atome, Zeitschrift Für Physik. 5 (1921) 17–26. https://doi.org/10.1007/BF01349680.

[64] I.G. Richardson, The importance of proper crystal-chemical and geometrical reasoning demonstrated using layered single and double hydroxides, Acta Crystallogr B Struct Sci Cryst Eng Mater. 69 (2013) 150–162. https://doi.org/10.1107/S205251921300376X.

[65] I.G. Richardson, Zn- and Co-based layered double hydroxides: prediction of the ıt a parameter from the fraction of trivalent cations and ıt vice versa, Acta Crystallographica Section B. 69 (2013) 414–417. https://doi.org/10.1107/S2052519213017545.

[66] A. Faour, C. Mousty, V. Prevot, B. Devouard, A. De Roy, P. Bordet, E. Elkaim, C. Taviot-Gueho, Correlation among Structure, Microstructure, and Electrochemical Properties of NiAl–CO3 Layered Double Hydroxide Thin Films, J. Phys. Chem. C. 116 (2012) 15646–15659. https://doi.org/10.1021/jp300780w.

[67] K. Page, T. Proffen, S. Mclain, B. Clausen, T. Darling, J. TenCate, S.-Y. Lee, E. Ustundag, Atomic pair distribution analysis of materials containing crystalline and amorphous phases, Zeitschrift Fur Kristallographie. 220 (2005). https://doi.org/10.1524/zkri.2005.220.12.1002.

[68] S. Krivovichev, V. Yakovenchuk, E. Zhitova, A. Zolotarev, Y. Pakhomovsky, G. Ivanyuk, Crystal chemistry of natural layered double hydroxides. 2. Quintinite-1M: First evidence of a monoclinic polytype in M2+-M3+ layered double hydroxides, Mineralogical Magazine. 74 (2010). https://doi.org/10.1180/minmag.2010.074.5.833.

[69] P. Bordet, Local structure studies using the pair distribution function, EPJ Web of Conferences. 104 (2015) 01003. https://doi.org/10.1051/epjconf/20159901003.

[70] J.-F. Boily, X. Song, Direct identification of reaction sites on ferrihydrite, Communications Chemistry. 3 (2020) 79. https://doi.org/10.1038/s42004-020-0325-y.

[71] Y. Tang, F.M. Michel, L. Zhang, R. Harrington, J.B. Parise, R.J. Reeder, Structural Properties of the Cr(III)−Fe(III) (Oxy)hydroxide Compositional Series: Insights for a Nanomaterial “Solid Solution,” Chem. Mater. 22 (2010) 3589–3598. https://doi.org/10.1021/cm1000472.

[72] A.A.A. Ahmed, Z.A. Talib, M.Z. Hussein, M.H. Flaifel, N.M. Al-Hada, Influence of Zn/Fe Molar Ratio on Optical and Magnetic Properties of ZnO and $ZnFe_2O_4$ Nanocrystal as Calcined Products of Layered Double Hydroxides, Journal of Spectroscopy. 2014 (2014) 1–6. https://doi.org/10.1155/2014/732163.

[73] S. Mandal, S. Mayadevi, B.D. Kulkarni, Adsorption of Aqueous Selenite [Se(IV)] Species on Synthetic Layered Double Hydroxide Materials, Ind. Eng. Chem. Res. 48 (2009) 7893–7898. https://doi.org/10.1021/ie900136s.

[74] L. Adlnasab, M. Ezoddin, M. Shabanian, B. Mahjoob, Development of ferrofluid mediated CLDH@Fe3O4@Tanic acid- based supramolecular solvent: Application in air-assisted dispersive micro solid phase extraction for preconcentration of diazinon and metalaxyl from various fruit juice samples, Microchemical Journal. 146 (2019) 1–11. https://doi.org/10.1016/j.microc.2018.12.020.

[75] K.M. Parida, L. Mohapatra, Carbonate intercalated Zn/Fe layered double hydroxide: A novel photocatalyst for the enhanced photo degradation of azo dyes, Chemical Engineering Journal. 179 (2012) 131–139. https://doi.org/10.1016/j.cej.2011.10.070.

[76] U. Schwertmann, Dr. R. M. Cornell, Iron Oxides in the Laboratory: Preparation and Characterization, Second edition, WILEY-VCH Verlag GmbH, 2000.

[77] J.-P. Jolivet, C. Chanéac, E. Tronc, Iron oxide chemistry. From molecular clusters to extended solid networks, Chem. Commun. (2004) 477–483. https://doi.org/10.1039/B304532N.

[78] F. Scholz, H. Kahlert, The calculation of the solubility of metal hydroxides, oxide-hydroxides, and oxides, and their visualisation in logarithmic diagrams, ChemTexts. 1 (2015) 7. https://doi.org/10.1007/s40828-015-0006-0.

[79] C. Liu, Z. Zhu, F. Li, T. Liu, C. Liao, J.-J. Lee, K. Shih, L. Tao, Y. Wu, Fe(II)-induced phase transformation of ferrihydrite: The inhibition effects and stabilization of divalent metal cations, Chemical Geology. 444 (2016) 110–119. https://doi.org/10.1016/j.chemgeo.2016.10.002.

[80] G.A. Waychunas, C.C. Fuller, J.A. Davis, J.J. Rehr, Surface complexation and precipitate geometry for aqueous Zn(II) sorption on ferrihydrite: II. XANES analysis and simulation, Geochimica et Cosmochimica Acta. 67 (2003) 1031–1043. https://doi.org/10.1016/S0016-7037(02)01280-2.

[81] S. Islam, S. Das, G. Mishra, B. Das, A. Malakar, I. Carlomagno, C. Meneghini, G. De Giudici, L.P.L. Gonçalves, J.P.S. Sousa, Y.V. Kolen'ko, A.C. Kuncser, S. Ray, Coagulating and flocculating ferrihydrite: application of zinc acetate salt, Environ. Sci.: Water Res. Technol. 6 (2020) 2057–2064. https://doi.org/10.1039/D0EW00357C.

[82] M. Nachtegaal, D.L. Sparks, Effect of iron oxide coatings on zinc sorption mechanisms at the clay-mineral/water interface, Journal of Colloid and Interface Science. 276 (2004) 13–23. https://doi.org/10.1016/j.jcis.2004.03.031.

[83] M. Stec, B. Jagustyn, K. Słowik, M. Sciazko, T. Iluk, Influence of High Chloride Concentration on pH Control in Hydroxide Precipitation of Heavy Metals, Journal of Sustainable Metallurgy. 6 (2020). https://doi.org/10.1007/s40831-020-00270-x.

[84] S. Cousy, N. Gorodylova, L. Svoboda, J. Zelenka, Influence of synthesis conditions over simonkolleite/ZnO precipitation, Chemical Papers. 71 (2017) 2325–2334. https://doi.org/10.1007/s11696-017-0226-4.

[85] A. Moezzi, M. Cortie, A. McDonagh, Transformation of zinc hydroxide chloride monohydrate to crystalline zinc oxide, Dalton Trans. 45 (2016) 7385–7390. https://doi.org/10.1039/C5DT04864H.

[86] J.W. Boclair, P.S. Braterman, Layered Double Hydroxide Stability. 1. Relative Stabilities of Layered Double Hydroxides and Their Simple Counterparts, Chem. Mater. 11 (1999) 298–302. https://doi.org/10.1021/cm980523u.

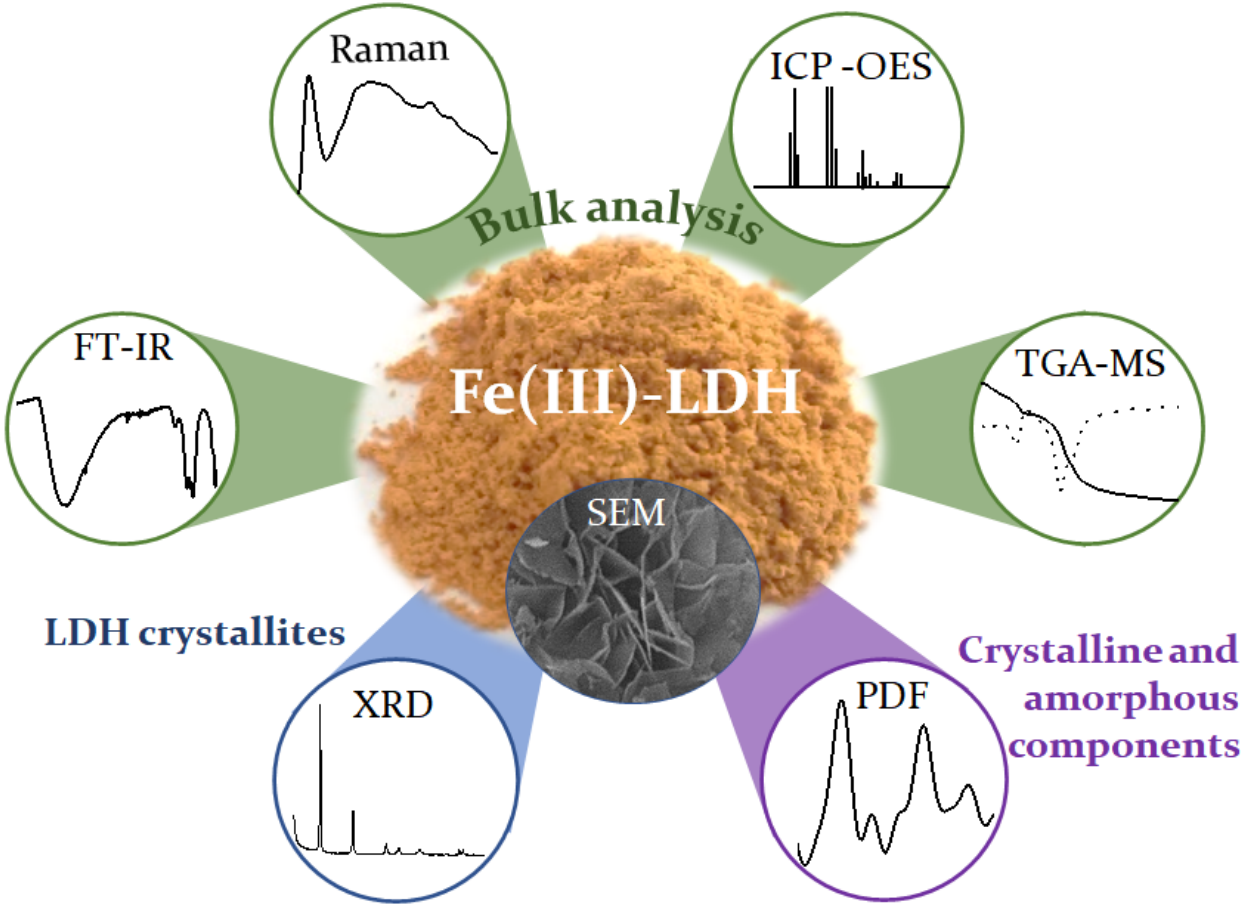
Raman
ICP -OES
Bulk analysis
FT-IR
Fe(III)-LDH
TGA-MS
SEM
LDH crystallites
XRD
PDF
Crystalline and amorphous components